Check for updates

Reduction of 4-nitrophenol and 2-nitroaniline using immobilized CoMn$_2$O$_4$ NPs on lignin supported on FPS

Yuning Chen,[a] Li Feng [ID] *[a] and Seyed Mohsen Sadeghzadeh [ID] *[b]

In the present work, fibrous phosphosilicate (FPS) was functionalized by using octakis[3-(3-aminopropyltriethoxysilane)propyl]octasilsesquioxane (APTPOSS) groups that act as strong performers. In this regard, the nanoparticles of CoMn$_2$O$_4$ were dispersed, properly, on FPS microsphere (CoMn$_2$O$_4$/APTPOSS@FPS) fibers. Agricultural and industrial waste waters contain nitrophenols. They are amongst the most common organic pollutants. In water, low concentrations are harmful to human health and aquatic life owing to the potential mutagenic and carcinogenic influences of nitrophenols. 4-Nitrophenol (4-NP), as well as 2-nitroaniline (2-NA), are known hazardous toxic waste contaminants and are included in the United States Environmental Protection Agency (USEPA) list. Thus, to eliminate them, novel methods are necessary. In addition, *o*-phenylenediamine (*o*-PDA) and 4-aminophenol (4-AP) are considered as significant intermediates for the synthesis of dyes and drugs, which are synthesized from 2-NA and 4-NP. Nanoparticles of CoMn$_2$O$_4$/APTPOSS@FPS utilized for the reduction of 2-NA and 4-NP, increase the efficiency of the reaction with considerable chemoselectivity. The results showed that the P and O atoms of lignin-FPS gold nanoparticles (NPs) were stable and the morphology and structure of FPS increased the catalytic activity.

[a]*School of Civil and Transportation Engineering, Guangdong University of Technology, No. 100, Waihuan Xi Road, Guangzhou Higher Education Mega Center, Panyu District, Guangzhou 510006, Guangdong, China. E-mail: fl19860314@126.com*
[b]*Young Researchers and Elite Club, Neyshabur Branch, Islamic Azad University, Neyshabur, Iran. E-mail: seyedmohsen_sadeghzadeh@yahoo.com*

Introduction

In recent years, green chemistry has been highly considered as being able to overcome environmental pollution originating from the world's population.[1–7] In aqueous solutions, the approach of reducing harmful organic solvents for transforming organic debris in reusable mixtures by using less toxic means has attracted a great response from scientific centers. Many studies have been performed to determine the availability of nitroaromatic materials. Agricultural and industrial waste waters contain nitrophenols, which are amongst the most common organic pollutants.[8,9] Low concentrations of nitrophenols in water are harmful to human health and aquatic life owing to the potential carcinogenic and mutagenic effects of nitrophenols.[10,11] Therefore, 2-nitroaniline (2-NA) and 4-nitrophenol (4-NP), which are hazardous and toxic waste pollutants, are included on the United States Environmental Protection Agency (USEPA) list.[12–16] Therefore, developing effective approaches to eliminate them is an important task. In addition, for the production of dyes and drugs that can be synthesized

from 4-NP and 2-NA, *o*-phenylenediamine (*o*-PDA) and 4-aminophenol (4-AP) are important intermediates.[17–21]
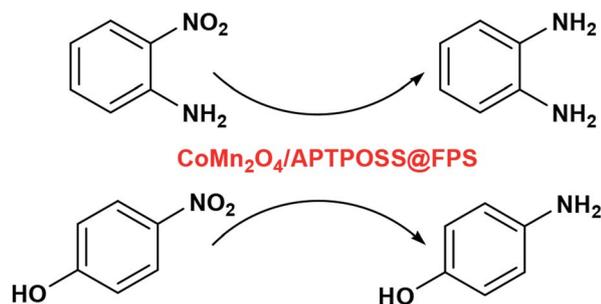
It has been reported in the literature that in comparison to transition metal oxides such as Co and Mn, valuable metal catalysts such as Pt, Pd, Au, and Ag demonstrate a greater activity.[22–26] However, valuable metal catalysts have many inevitable drawbacks such as a tendency to be easily poisoned, there are limited resources, and they have a high cost. As they have a high specific surface area, are exotic, and have reduced dimensionality properties, two-dimensional nanosheets have been used for the design of novel electrocatalysts for carbon dioxide reduction.[27–34] Borophene has been introduced as a novel 2D material under active investigation owing to its fascinating and diverse attributes, as well as its potential.[35] It has been demonstrated that the properties of borophene can be improved and further developed by alloying it, amongst other factors. Allowing the opportunity to design novel functional catalysts or materials.

Significant efforts have been made for the expansion of efficient transition metal oxide catalysts with a high thermal stability and low costs for adapting noble metal catalysts.[36–39] Manganese and cobalt are recognized as the most promising among the transition metal oxides owing to their low price and adequate activities at relatively low temperatures. For toluene and benzene oxidation, scholars propose the following catalytic activity order: Mn$_3$O$_4$ > α-Mn$_2$O$_3$ > β-MnO$_2$. For total oxidation, Mn with a high valence is more active. The further addition of

Scheme 1 Reduction of 4-NP and 2-NA from alkylphenols in the presence of the CoMn$_2$O$_4$/APTPOSS@FPS NPs.

alkaline earth metals and alkali metals enhances the catalytic performance.[40–43]

The utilization of surfactants on soft templates simplifies the mesoporous phosphosilicate produced and the phosphosilicate fibers have a dendrimetric morphology. Phosphosilicates with this specific morphology were tested as support materials. For the reactants, in order to access the functional materials in terms of the adsorption and catalysis approaches, the apparent expansion of these silicas indicated a higher surface area. Moreover, fibrous phosphosilicate (FPS), which has intrinsic mesoporous properties, is thermally stable, and possesses a high activity. The FPS produced requires a microemulsion method that includes water, oils, and surfactants. Moreover, the FPS morphology and particle size can be managed by the use of many co-solvents and co-surfactants.[44–51]

In this way, the organic groups were replaced by silica groups. For proper stabilization and immobilization of the metal catalysts, we showed that octakis[3-(3-amino-propyltriethoxysilane)propyl]octasilsesquioxane (APTPOSS) is a highly efficient and powerful support. With this replacement, the strength of the catalytic structure was improved. This catalyst support was fabricated by FPS obstruction using APTPOSS (APTPOSS@FPS). Actually, APTPOSS@FPS is a nano labyrinth for holding the nanoparticle. It was determined that this particular property can be very beneficial for the design of silica-supported catalysts. The availability of the active sites may be considerably improved. In the present work, APTPOSS@FPS is utilized as a novel supporting material for stabilizing CoMn$_2$O$_4$ nanoparticles (NPs) and for achieving a CoMn$_2$O$_4$/APT-POSS@FPS nanocatalyst along with an improved high surface area and accessibility for the active sites. Moreover, as seen in Scheme 1, its utility was described for the catalytic reduction of 2-NA and 4-NP and it can be separated from the reaction mixture for reuse.

Experimental

General approach for the preparation of the FPS nanoparticles

Tetraethyl orthosilicate (TEOS) (2.08 g) and tripolyphosphate (TPP) (3.67 g) were dissolved in a solution of cyclohexane (30 mL) and 1-pentanol (1.5 mL). A stirred solution of cetylpyridinium bromide (CPB 1 g) and urea (0.5 g) in water (30 mL) was then added. The resulting mixture was continually stirred for

45 min at room temperature and then placed in a Teflon-sealed hydrothermal reactor and heated at 120 °C for 5 h. The FPS was then isolated by centrifugation, washed with deionized water and acetone, and dried in a drying oven.[45]

Synthesis of APTPOSS

Under a nitrogen atmosphere, 2 mmol ClPOSS and 20 mmol 3-aminopropyltriethoxysilane were transferred to a reaction vessel and the reaction solution was stirred at a temperature of 100 °C for 48 h. After that the mixture was cooled to 25 °C temperature and the solution was filtered and then washed with acetone and methanol.

General approach for the synthesis of nanoparticles of APTPOSS@FPS

2 mmol of the FPS NPs and 20 mL THF were mixed together in a beaker. After that, 20 mmol of NaH was dispersed into the mixture using ultrasonication. 0.5 g APTPOSS was added at 25 °C and stirred at 60 °C for another 16 h. The resulting products were gathered and then washed repeatedly using deionized water and ethanol. After that, the products were dried under a vacuum at a temperature of 60 °C for 2 h and stored for further use.

General approach for the synthesis of nanoparticles of CoMn$_2$O$_4$/APTPOSS@FPS

FPS/APTPOSS (0.1 g), 1.1 mL of aqueous 45 mM Mn(NO$_3$)$_2$·4H$_2$O and 45 mM Co(NO$_3$)$_2$·6H$_2$O were dissolved in distilled water. Then, 0.002 mol citric acid was added to the mixed solution. The pH of this solution was set to 9 using tetraethylenepentamine (TEPA) added drop-wise. In the second step, 0.002 mol of ethylene glycol was added to the solution as an agent for esterification. The synthesis of the porous solid mass can be enabled by enhancing the temperature and the evaporation of the gel-like solution. Ferula asafoetida gum was (1 g) added to achieved powders and these were calcinated at a temperature of 700 °C for around 3 h.

General approach for the reduction of 4-NP

In the first step, 40 μL of the aqueous 4-NP solution, 1.26×10^{-2} mol L^{-1}, was added to 2.5 mL water. After that, it was mixed with a freshly prepared aqueous 0.5 M NaBH$_4$ solution and a deep yellow solution was obtained. 0.4 mg of the catalyst was added into the obtained yellow solution and when this solution became colorless, the reaction was complete. The reaction progress was monitored using UV-vis absorption spectroscopy of the reaction mixture.

General approach for the reduction of 2-NA

A constant amount of the catalyst (1 mg) was added to 2.5 mL water, and this was then mixed with a 2-NA aqueous solution (40 μL, 1.26×10^{-2} mol L^{-1}) and a 0.5 M NaBH$_4$ solution was rapidly injected while stirring. The mixture color gradually vanished, showing the 2-NA reduction. By measuring the UV-vis
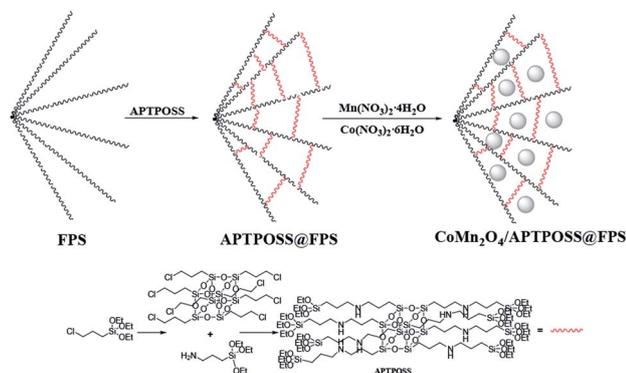
absorption spectra of the reaction mixture, the reaction trend was monitored.

Results and discussion

The nanoparticles of $CoMn_2O_4$/APTPOSS@FPS are produced using a simplistic three step method. Firstly, FPS is made by the simultaneous condensation and hydrolysis of TPP as well as TEOS. After that, the FPS fibers possess many P–OH and Si–OH groups on their surfaces. Therefore, to form APTPOSS@FPS, the FPS can be easily functionalized with APTPOSS. Lastly, the APTPOSS groups on the FPS can act as aggregation centers to enhance the metal NPs on the surface of FPS. In the case of FPS (Scheme 2), to retain the nanoparticles, we determined the best combination of the three structure of APTPOSS. These were characterized using energy-dispersive X-ray spectroscopy (EDX), scanning electron microscopy (SEM), X-ray diffractometry (XRD), atomic force microscopy (AFM), and transmission electron microscopy (TEM) analysis. It is important to note that the authenticity of the $CoMn_2O_4$/APTPOSS@FPS synthesis is mentioned in our previous study.

Fig. 1 shows the field emission scanning electron microscopy (FESEM) schema of FPS. It was determined that the FPS sample includes wall-like domains (as seen in Fig. 1a) and the wall sizes were fixed (Fig. 1c). Further investigation of the mentioned schemas shows that the material had dendrimetric fibers possessing a thickness in the range of 10–15 nm. It was adjusted in three dimensions for forming walls, which can easily facilitate availability owing to the existing high surface area. The fibers of FPS consist of different groups of Si–OH and P–OH on these levels. The groups of Si–OH and P–OH over the surface may act as association centers in the case of the growth of NPs of $CoMn_2O_4$ over the FPS level. Fig. 1b and d show the FESEM and TEM images in the case of the $CoMn_2O_4$ NPs. As can be seen, the as-prepared metal NPs were spherical and did not show obvious aggregation. The diameter of the NPs of $CoMn_2O_4$ was about 10 nm. It should be noted that the morphology of the nanoparticles is near-wall.

Fig. 2 shows the XRD spectra of the FPS and $CoMn_2O_4$/APTPOSS@FPS NPs. The XRD spectra of the FPS NPs indicates
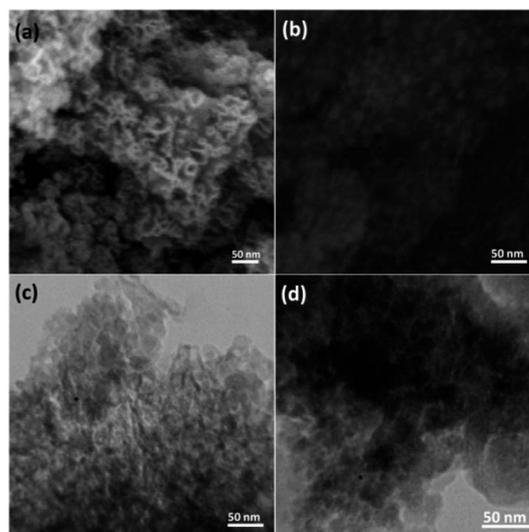

Fig. 1 FESEM images of the FPS NPs (a) and $CoMn_2O_4$/APTPOSS@FPS NPs (b); and TEM images of the FPS NPs (c) and $CoMn_2O_4$/APTPOSS@FPS NPs (d).

a number of crystalline peaks as stated in a previous study.[52] As seen in Fig. 2, the total diffraction peaks completely matched those of the pure fluorite $CoMn_2O_4$ and no impurities exist in this image.[53] For the $CoMn_2O_4$/APTPOSS@FPS nanoparticles, new peaks reflecting the $CoMn_2O_4$ crystal confirmed the proper growth of the $CoMn_2O_4$ particles on the FPS surface.

As seen in Fig. 3, to obtain a high level of detail, the EDX spectrum was characterized to reveal the purity of the $CoMn_2O_4$/APTPOSS@FPS nanoparticles, which have a fibrous shape. The EDX picture additionally proved the presence of P and Si in similar weight ratios affirming the proper cooperation of TPP and TEOS in the structure of FPS. The existence of O, Mn, and Co demonstrates that the fibrous $CoMn_2O_4$ specimen has been fabricated. The roughness of the nanoparticles of $CoMn_2O_4$/APTPOSS@FPS was determined using AFM analysis. Fig. 4 shows the topographic image. As observed in Fig. 4, the regions
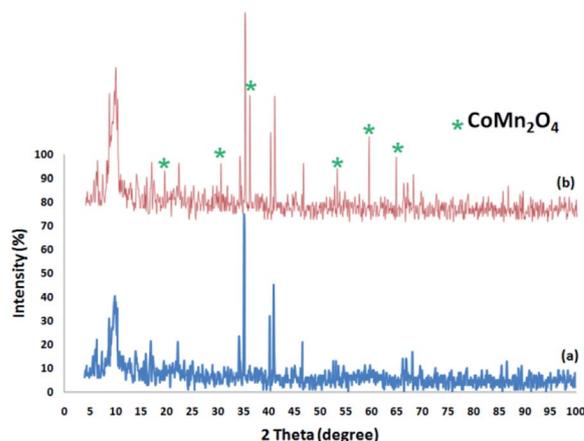

Scheme 2 Schematic illustration of the synthesis of $CoMn_2O_4$/APTPOSS@FPS.

Fig. 2 XRD analysis of (a) the FPS NPs, and (b) the $CoMn_2O_4$/APTPOSS@FPS NPs.
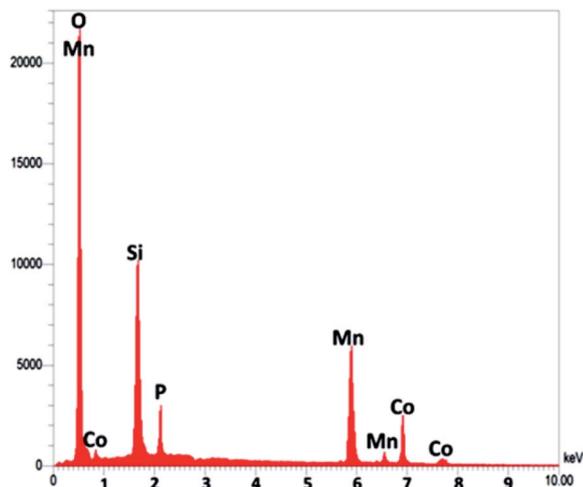
Fig. 3 EDX spectrum of CoMn$_2$O$_4$/APTPOSS@FPS.
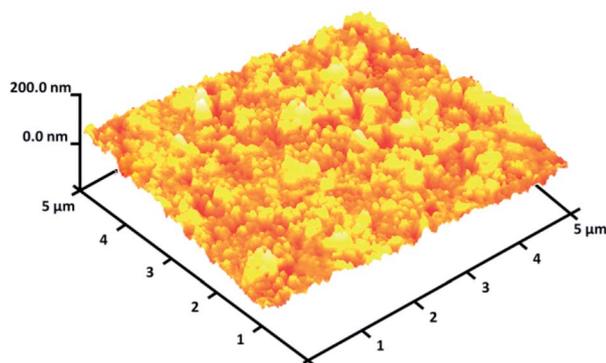

Fig. 4 Three-dimensional AFM images of the CoMn$_2$O$_4$/APT-POSS@FPS NPs.

with a greater height, shown using the brighter yellowish white color, improved with the reducing thickness (T)/width (W), indicating the enhancement in the roughness of the catalyst.

For FPS, the N$_2$ adsorption–desorption isotherms of the nanostructure of FPS demonstrated a specific type IV curve. The Barrett–Joyner–Halenda (BJH) pore diameter, total pore volume, and Brunauer–Emmett–Teller (BET) surface area, were found to be 7.92 nm, 0.86 cm^3 g^{-1}, and 213 m^2 g^{-1} respectively, while the corresponding results were 7.21 nm, 0.79 cm^3 g^{-1}, and 204 m^2 g^{-1} for APTPOSS@FPS. In comparison to APTPOSS@FPS, no considerable change was seen in the pore volumes of FPS.

Table 1 Structural parameters of FPS, APTPOSS@FPS, and CoMn$_2$O$_4$/APTPOSS@FPS materials determined from the nitrogen sorption experiments

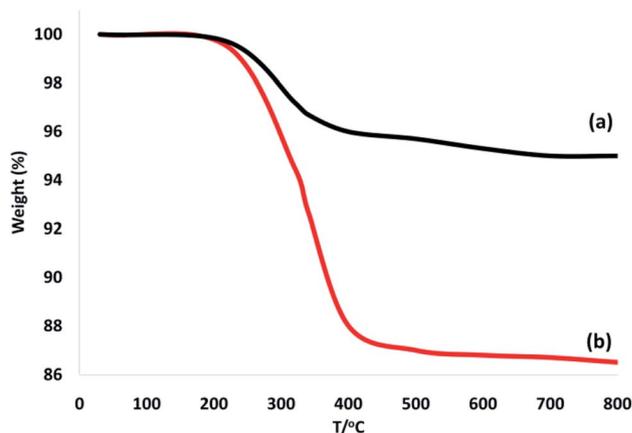| Catalyst	S_{BET} (m^2 g^{-1})	V_t (cm^3 g^{-1})	D_{BJH} (nm)
FPS	213	0.86	7.92
APTPOSS@FPS	204	0.79	7.21
CoMn$_2$O$_4$/APTPOSS@FPS	124	0.42	1.34

Fig. 5 TGA diagram of (a) FPS, and (b) the CoMn$_2$O$_4$/APTPOSS@FPS NPs.

Table 1 shows that this can be ascribed to the fibrous structure. The formation of the CoMn$_2$O$_4$ NPs caused a further decrease, however, there was a less pronounced reduction in the porosity characteristics (Table 1, entry 3). The formation of CoMn$_2$O$_4$ NPs upon reduction caused further, but less pronounced, reduction of the porosity characteristics. The reduction of the pore volume upon the formation of particles was marked, in particular, for CoMn$_2$O$_4$/APTPOSS@FPS from 0.42 cm^3 g^{-1} and APTPOSS@FPS to 0.79 cm^3 g^{-1}. The obtained result indicates that the CoMn$_2$O$_4$ NPs form directly in the APTPOSS@FPS derivative pores.

To confirm the thermal stability of the CoMn$_2$O$_4$/APTPOSS@FPS NPs, thermogravimetric analysis was performed under temperatures in the range of 25 to 800 °C (Fig. 5). The weight loss below the temperature of 250 °C was caused by the elimination of the chemisorbed and physisorbed solvent over the silica material surface. The provided organic weight losses for CoMn$_2$O$_4$/APTPOSS@FPS are 7.8%. Based on these results, the good grafting yields of the organic compounds on the NPs were corroborated.

In addition, the FPS spectra revealed a further peak at about 1483 cm^{-1} that can be ascribed to the phosphate moiety obtained from TPP. In the FPS spectrum, the main peak was the additional peak observed at 1232 cm^{-1} that can be attributed to
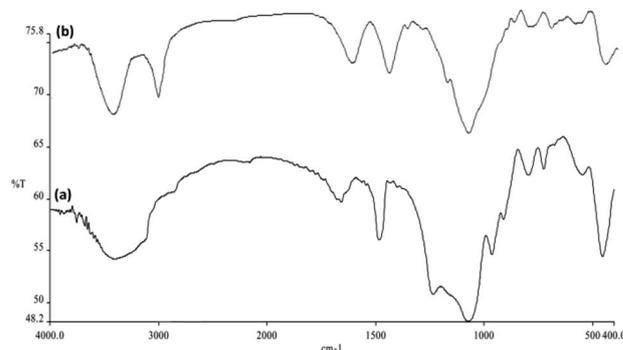

Fig. 6 Fourier transform infrared spectroscopy (FTIR) spectra of (a) FPS NPs, and (b) CoMn$_2$O$_4$/APTPOSS@FPS NPs.

the –P=O stretching vibration showing the presence of the phosphate group. The shoulder at 1108 cm^{-1} and the band at 963 cm^{-1} could be because of the longitudinal optimal (LO) and transverse optical (TO) modes of the asymmetric stretching vibration of the Si–O–P bonds, respectively. The bands at around 724 and 795 cm^{-1} are considered to be a result of the asymmetric stretching of the bridging oxygen atoms that are bonded to the phosphorus atom, which provide appropriate proof of the presence of TPP and TEOS in the FPS structure (Fig. 6a). The bands observed at 2956 cm^{-1} are assigned to the

C–H stretching of the aliphatic moieties (Fig. 6b). These results indicated that APTPOSS had been successfully introduced onto the surface of the FPS.

The catalytic efficiency of the NPs of CoMn$_2$O$_4$/APTPOSS@FPS was studied by utilizing the 4-NP reduction to 4-AP in the presence of NaBH$_4$ as the probe reaction. The development approach using the time duration of the reaction for the reduction of 4-NP to 4-AP was analyzed using UV-vis spectroscopy. Fig. 7a shows that the 4-NP solution represents the proper absorption peak at 300 nm and this was dramatically redshifted to 400 nm. The addition of 1 mg of the NPs of CoMn$_2$O$_4$/APTPOSS@FPS to the system caused the peak intensity of 4-NP at 400 nm to decrease in addition to the concomitant enhancement of the peaks relating to 4-AP at 300 nm. This is caused by the formation of the 4-NP ion upon the addition of NaBH$_4$. An aqueous solution of NaBH$_4$ is basic, which induces the formation of the 4-nitrophenoxide anion in solution. Fig. 7b shows that the reaction rapidly progresses by the conversion of more than 99.8% in a reaction time of around 100 s. We also used the CoMn$_2$O$_4$/APTPOSS@FPS NPs to determine the catalytic reduction of 2-NA according to the above mentioned outcomes. The reduction of 2-NA can also be easily monitored because the product for the reduction was only. The reaction progress may be found by calculating the variation in the UV-vis absorbance. The 2-NA yellow colored solution presented two distinguished absorption peaks at 280 and 400 nm. By adding the NaBH$_4$ solution, the intensity of the aforementioned peaks

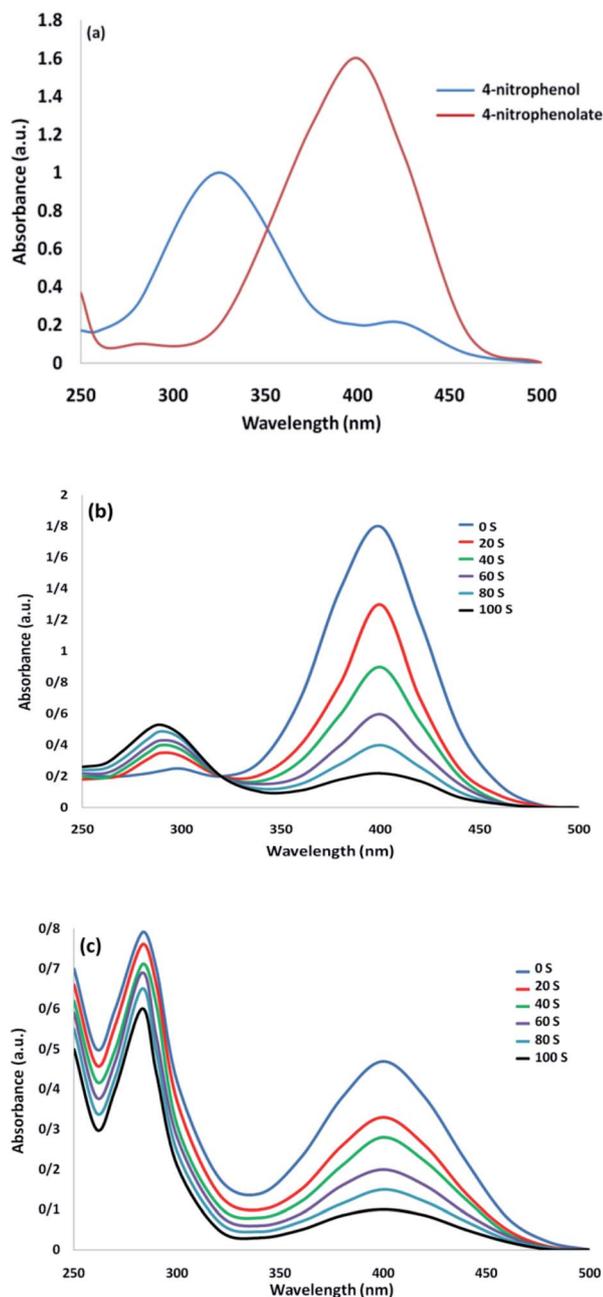Fig. 7 UV-vis spectra of (a) 4-NP before and after adding the solution of NaBH$_4$; (b) the consecutive reduction of 4-NP to 4-AP; as well as (c) 2-NA to o-PDA on the CoMn$_2$O$_4$/APTPOSS@FPS NPs catalyst.
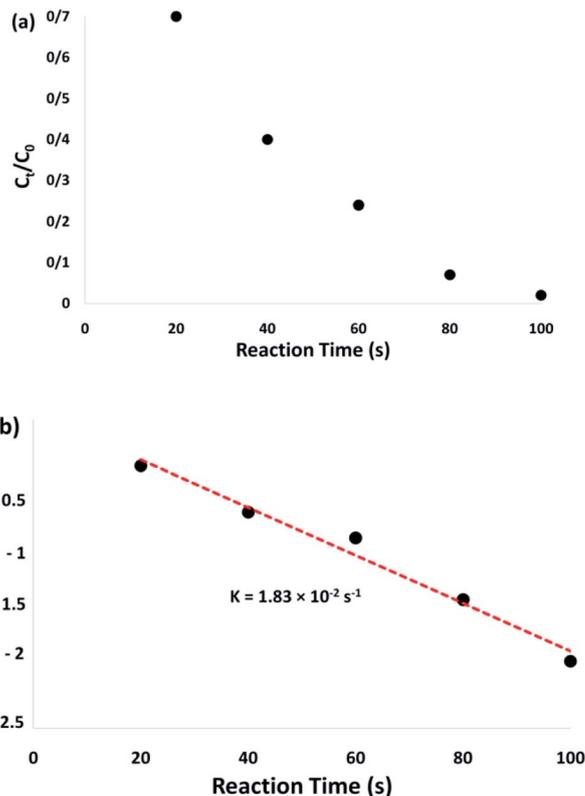

Fig. 8 Plots of C_t/C_0 (a) and ln(C_t/C_0) (b) versus reaction time for the reduction of 4-NP over the CoMn$_2$O$_4$/APTPOSS@FPS NPs.

did not reduce. Nevertheless, as can be seen in Fig. 7c, the intensity of the above mentioned peaks gradually reduced upon the addition of NPs of $CoMn_2O_4$/APTPOSS@FPS to a $NaBH_4$ and 2-NA mixed solution.

The conversion of the reaction was predicted from the C_t/C_0 and used to evaluate the relative intensity of the UV-vis absorbance (A_t/A_0) (at 400 nm). C_t represents the 4-NP concentration at the reaction time (t). The C_0 shows the primary concentration. As illustrated in Fig. 8a, the mean amount of the reaction conversions with standard deviation are given. Fig. 8b shows the linear correlation with the reaction time and the $\ln(C_t/C_0)$ shows that the reaction is first-order considering the 4-NP reduction. Fig. 8b shows the linear correlation between the reaction time and $\ln(C_t/C_0)$. As seen, with respect to the reduction of 4-NP, the reaction is first-order. Hence, the kinetic equation for this catalytic reduction reaction can be denoted as $\ln(C_t/C_0) = -kt$. In this relationship, t shows the reaction time and k represents the apparent first-order rate constant (s^{-1}). For the $CoMn_2O_4$/APTPOSS@FPS nanoparticle catalyzed 4-NP reduction, the k (reaction rate constant) is predicted to be 1.83×10^{-2} s^{-1}. The activity parameter, $k' = k/M$, is presented, for quantitative comparison, and introduced as the ratio of k to the weight of the catalyst used.[54] Here, M shows the total mass of the catalyst, which is used during the reaction. Therefore, the reaction rate constants per unit mass are predicted to be 18.3 s^{-1} g^{-1} for the 4-NP reduction.

Table 2 shows the activity factors utilized to compare the catalytic activity of $CoMn_2O_4$/APTPOSS@FPS against the Cu, Ag, Co, and Ni nanoparticle based catalysts used for the reduction of 4-NP. As observed in Table 2, k and k' for the $CoMn_2O_4$/APTPOSS@FPS nanocatalyst are greater than those reported for the p(AMPS)-Cu, p(AMPS)-Co, and p(AMPS)-Ni catalysts. Based on previous works, the nanoparticles of p(AMPS)-Co NPs[56] and p(AMPS)-Ni[55] have activity factors of around 0.04 and 0.019 s^{-1} g^{-1}, respectively. The rate constant k' of p(AMPS)-Cu is equal to 0.172 s^{-1} g^{-1},[57] which is greater than the TAC-Ag-1 catalyst (1.3 s^{-1} g^{-1}) and the Ag doped carbon spheres catalyst (1.69 s^{-1} g^{-1}), as well as the Fe_3O_4@SiO_2–Ag NPs (7.67 s^{-1} g^{-1}).[58–60] The catalytic activity of the nanocatalyst of $CoMn_2O_4$/APTPOSS@FPS achieved here is 18.3 s^{-1} g^{-1}, which is considerably more than the catalytic activities of the nanoparticle based catalysts
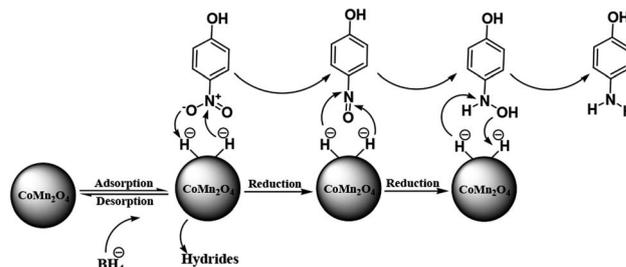
Scheme 3 A plausible mechanism for the reduction of p-nitrophenol catalyzed by the $CoMn_2O_4$/APTPOSS@FPS NPs catalyst in the presence of $NaBH_4$.

introduced above; therefore the nanocatalyst of $CoMn_2O_4$/APTPOSS@FPS presents a preferable catalytic activity in terms of the reduction reactions.

Scheme 3 shows a representation of the reaction along with the activation of the hydrides on the surface of the catalyst and their transfer to the nitro group. Based on previous works, during the reduction of nitroarenes by $NaBH_4$ catalyzed using nanoparticles of $CoMn_2O_4$, the cleavage of the B–H bond is the rate-determining step giving the $CoMn_2O_4$–H type. In the metal–hydrogen structure, the charged hydrogen, which is negative, may attack the positively charged nitrogen, quickly, which is in the nitro group of the nitrophenols. Therefore, the nitro group was decreased to the nitroso group along with the reductive addition of two hydrogen atoms to form hydroxylamine. In the last step, the hydroxylamine was further decreased to the aniline derivative.

The magnetic properties of the $CoMn_2O_4$/APTPOSS@FPS NPs can improve the efficient recovery of the reaction mixture after the reaction. The activity of the recycled catalyst was evaluated over ten consecutive cycles to determine any considerable loss in the catalytic activity. Fig. 9 shows that after the reaction, the catalyst can be separated by utilizing filtration. After that we washed it with methanol and then dried it using a pump. To further evaluate the stability of the catalyst, we also performed kinetic investigations for the first 100 s in four recycling tests. Fig. 10 shows that the conversion continues to be enhanced by the increasing reaction time, reaching approximately 95% after 100 s. The kinetic curves in the case of the

Table 2 Comparing catalytic activities to the 4-NP reduction by catalysts

Catalysts	Catalyst (mg)	k^a (s^{-1})	k/M^b $(s^{-1}$ $g^{-1})$
p(AMPS)-Co[46]	50	2×10^{-3}	0.04
p(AMPS)-Ni[47]	50	9.38×10^{-4}	0.019
TAC-Ag-1.0 (ref. 48)	4.0	5.19×10^{-3}	1.3
Ag/C spheres[49]	1.0	1.69×10^{-3}	1.69
Fe_3O_4@SiO_2–Ag[50]	1.0	7.67×10^{-3}	7.67
p(AMPS)-Cu[51]	10	1.72×10^{-3}	0.172
$CoMn_2O_4$/APTPOSS@FPS	1.0	1.83×10^{-2}	18.3

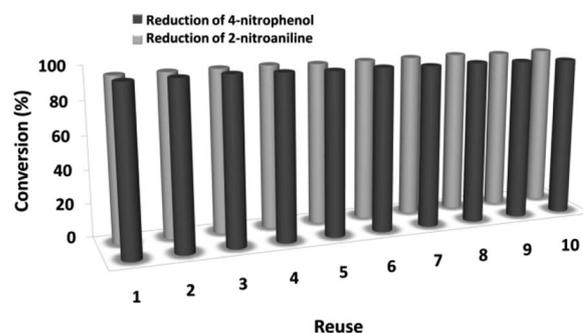^{a} The reaction rate constant. ^{b} The reaction rate constant per total weight of catalyst used.

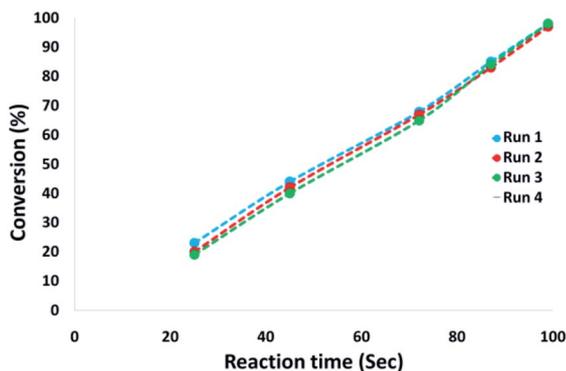Fig. 9 The reusability of catalysts for the reduction of 4-NP and 2-NA with $NaBH_4$.

Fig. 10 Kinetic data for the catalyst followed by four recycling runs.

Fig. 12 Reaction kinetics, Hg(0) poisoning, and hot filtration studies for the reduction of p-nitrophenol.

four recycling runs were almost overlapping each other, this shows that during these recycle runs the catalyst was not deactivated. Moreover, the $CoMn_2O_4$ value leached into the solution for the reduction of p-nitrophenol after each run was analyzed by taking into account the inductively coupled plasma (ICP). In each turn, the catalyst demonstrated very little leaching, for example, after the tenth run, 0.8% metal leaching was discovered, thus indicating the consistent reaction states as shown in Fig. 11.

Moreover, we conducted a complete analysis to clarify the heterogeneous nature of the catalyst. In the first step, we performed a hot filtration experiment in terms of the reduction of p-nitrophenol under optimum conditions. The catalyst is filteration deleted *in situ* after around 49% for 50 s removal. Moreover, the reactants tolerated further reactions. Our results proved that the free catalyst remnant was still slightly active, after removing the heterogeneous catalyst. A conversion of around 41% was achieved after 100 s of p-nitrophenol reduction. It was demonstrated that the catalyst acted heterogeneously in the reaction and only a slight amount of leaching occurred during the reaction. In the second step, mercury poisoning analysis was also performed to determine the heterogeneous pattern of the catalyst. Mercury(0) was imbibed as a metal for utilizing synthesis and dramatically deactivated the metal catalyst on the active surface, thus inhibiting the catalyst activity. The results of our experiments proved the activity of the heterogeneous catalyst. This analysis was performed using the above mentioned model of the reaction at
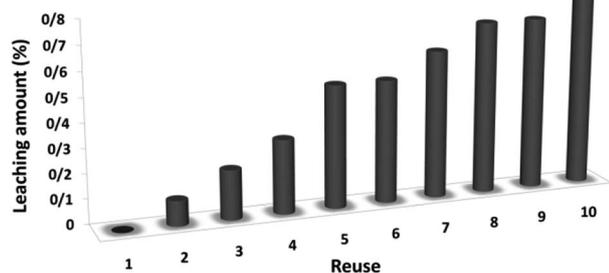
optimum conditions. About 300 molar mercury was released to the reaction compound during the reaction (after 50 s). The reaction was stirred for more than 100 s and no further conversion was observed after 100 s from the catalyst being poisoned. Fig. 12 shows the kinetics scheme in the case of the reaction in the presence of Hg(0). The negative outcomes achieved from the heterogeneity experiments (hot filtration and Hg(0) poisoning) suggested that the solid catalyst was actually heterogeneous. In addition, no obtainable $CoMn_2O_4$ leaching occurred during p-nitrophenol reduction.

Finally, we studied the structure of the recovered catalyst after the tenth run in terms of the p-nitrophenol reduction at the indicated optimum conditions (Fig. 13) to determine whether the structure of the recovered catalyst was maintained or not. In the case of the catalyst, the EDX pattern showed the $CoMn_2O_4$ elements were completely exhausted after the tenth run and after that their oxidation state was identical to that of the fresh catalyst (Fig. 13a). As observed in Fig. 13b, the XRD pattern for the reproduced catalyst demonstrated that the
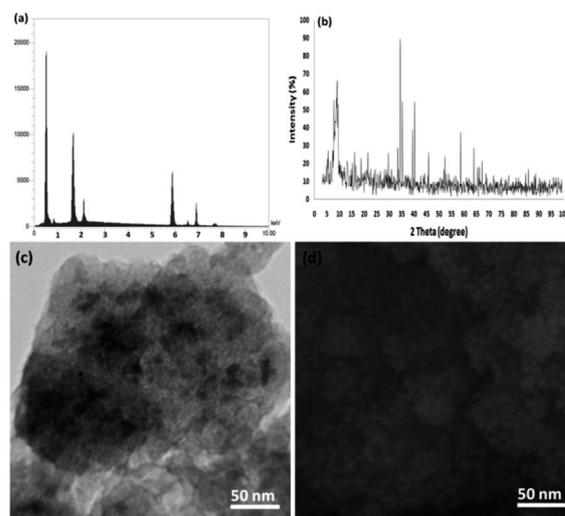

Fig. 11 Recyclability of the catalyst for the reduction of p-nitrophenol.

Fig. 13 (a) EDX, (b) XRD, (c) TEM, and (d) FESEM images of the recovered $CoMn_2O_4$/APTPOSS@FPS NPs after the tenth run for the reduction of p-nitrophenol.

fatigued catalytic structure remained completely intact during recycling. The SEM and TEM images analysis revealed further data in the case of the fibrous NPs of CoMn$_2$O$_4$/APTPOSS@FPS. As seen in Fig. 13c and d, the TEM and SEM images for the new fibrous nanoparticles of CoMn$_2$O$_4$/APTPOSS@FPS, and the fibrous NPs of CoMn$_2$O$_4$/APTPOSS@FPS reused ten times are demonstrated. The structure of the fibrous-like catalyst can be still observed after being reused ten times. The same structure was observed in the fresh fibrous nanoparticles of CoMn$_2$O$_4$/APTPOSS@FPS and the CoMn$_2$O$_4$/APTPOSS@FPS reused ten times, indicating the excellent recyclability.

Conclusions

In this paper, we synthesized and suggested a novel, nano catalyst, the CoMn$_2$O$_4$/APTPOSS@FPS NPs. This nanocatalyst, along with the NPs of CoMn$_2$O$_4$ as the active sites, may allow the use of CoMn$_2$O$_4$ NPs to be decreased without decreasing the catalytic activity. In addition, this may confer heterogeneous characteristics to the nanocatalyst, allowing the catalyst to be simply retrieved for reuse. The CoMn$_2$O$_4$/APTPOSS@FPS NPs showed appropriate catalytic activity in terms of 4-NP and 2-NA reduction. This could be owed to the high availability of the CoMn$_2$O$_4$/APTPOSS@FPS NPs support material as well as the low aggregation of the CoMn$_2$O$_4$ NPs on the APTPOSS@FPS support. In addition, one can reuse the CoMn$_2$O$_4$/APT-POSS@FPS NPs at least ten times owing to the prevention of leaching of the CoMn$_2$O$_4$ NPs from the CoMn$_2$O$_4$/APT-POSS@FPS NPs (without resulting in any reduction in the catalytic activity).

Conflicts of interest

There are no conflicts to declare.

Acknowledgements

Notes and references

1 J. Zhang, G. Chen, M. Chaker, F. Rosei and D. Ma, *Appl. Catal., B*, 2013, **132**, 107–115.

2 F. Cardenas-Lizana, D. Lamey, N. Perret, S. Gomez-Quero, L. Kiwi-Minsker and M. A. Keane, *Catal. Commun.*, 2012, **21**, 46–51.

3 Z. Y. Zhang, C. L. Shao, P. Zou, P. Zhang, M. Y. Zhang, J. B. Mu, Z. C. Guo, X. H. Li, C. H. Wang and Y. C. Liu, *Chem. Commun.*, 2011, **47**, 3906–3908.

4 M. Zarejousheghani, M. Moeder and H. Borsdorf, *Anal. Chim. Acta*, 2013, **798**, 48–55.

5 X. Li, X. Wang, S. Song, D. Liu and H. Zhang, *Chem.–Eur. J.*, 2012, **18**, 7601–7607.

6 F. Coccia, L. Tonucci, D. Bosco, M. Bressan and N. d'Alessandrro, *Green Chem.*, 2012, **14**, 1073–1078.

7 M. Yoosefian, A. Mola, E. Fooladi and S. Ahmadzadeh, *J. Mol. Liq.*, 2017, **225**, 34–41.

8 N. Etminan, M. Yoosefian, H. Raissi and M. Hakimi, *J. Mol. Liq.*, 2016, **214**, 313–318.

9 M. Yoosefian, *Appl. Surf. Sci.*, 2017, **392**, 225–230.

10 X. Le, Z. Dong, W. Zhang, X. Li and J. Ma, *J. Mol. Catal. A: Chem.*, 2014, **395**, 58–65.

11 X. Le, Z. Dong, X. Li, W. Zhang, M. Le and J. Ma, *Catal. Commun.*, 2015, **59**, 21–25.

12 O. A. O'Connor and L. Y. Young, *Environ. Toxicol. Chem.*, 1989, **8**, 853–862.

13 M. A. Oturan, J. Peiroten, P. Chartrin and A. J. Acher, *Environ. Sci. Technol.*, 2000, **34**, 3474–3479.

14 K. Li, Z. Zheng, X. Huang, G. Zhao, J. Feng and J. Zhang, *J. Hazard. Mater.*, 2009, **166**, 213–220.

15 Y. Zhang, X. Yuan, Y. Wang and Y. Chen, *J. Mater. Chem.*, 2012, **22**, 7245–7251.

16 S. Saha, A. Pal, S. Kundu, S. Basu and T. Pal, *Langmuir*, 2010, **26**, 2885–2893.

17 N. Sahiner, N. Karakoyun, D. Alpaslan and N. Aktas, *Int. J. Polym. Mater. Polym. Biomater.*, 2013, **62**, 590–595.

18 Y. Yang, Y. Guo, F. Liu, X. Yuan, Y. Guo, S. Zhang, W. Guo and M. Huo, *Appl. Catal., B*, 2013, **142–143**, 828–837.

19 M. M. Mohamed and M. S. Al-Sharif, *Appl. Catal., B*, 2013, **142–143**, 432–441.

20 M. Muniz-Miranda, *Appl. Catal., B*, 2014, **146**, 147–150.

21 H. Ozay, S. Kubilay, N. Aktas and N. Sahiner, *Int. J. Polym. Mater.*, 2011, **60**, 163–173.

22 B. C. H. Steele and A. Heinzel, *Nature*, 2001, **414**, 345–352.

23 G. Meng, G. Ma, Q. Ma, R. Peng and X. Liu, *Solid State Ionics*, 2007, **178**, 697–703.

24 Z. G. Liu, J. H. Ouyang and K. N. Sun, *Fuel Cells*, 2011, **11**, 153–157.

25 X. Cao, R. Vassen, W. Fischer, F. Tietz, W. Jungen and D. Stover, *Adv. Mater.*, 2003, **15**, 1438–1442.

26 Z. Salehi, S. Zinatloo-Ajabshir and M. Salavati-Niasari, *J. Mol. Liq.*, 2016, **222**, 218–224.

27 B. Song, Y. Zhou, H. M. Yang, J. H. Liao, L. M. Yang, X. B. Yang and E. Ganz, *J. Am. Chem. Soc.*, 2019, **141**, 3630–3640.

28 L. M. Yang, V. Bačić, I. A. Popov, A. I. Boldyrev, T. Heine, T. Frauenheim and E. Ganz, *J. Am. Chem. Soc.*, 2015, **137**, 2757–2762.

29 J. H. Liu, L. M. Yang and E. Ganz, *ACS Sustainable Chem. Eng.*, 2018, **6**, 15494–15502.

30 J. H. Liu, L. M. Yang and E. Ganz, *J. Mater. Chem. A*, 2019, **7**, 3805–3814.

31 J. H. Liu, L. M. Yang and E. Ganz, *J. Mater. Chem. A*, 2019, **7**, 11944–11952.

32 J. H. Liu, L. M. Yang and E. Ganz, *RSC Adv.*, 2019, **9**, 27710–27719.

33 Y. Yoo, G. D. Park and Y. C. Kang, *Energy Environ. Mater.*, 2019, **2**, 193–200.

34 L. Xu, L. M. Yang and E. Ganz, *Theor. Chem. Acc.*, 2018, **137**, 98.

35 Y. Liu, L. M. Yang and E. Ganz, *Condens. Matter*, 2019, **4**, 65.

36 Y. Ling, J. Chen, Z. Wang, C. Xia, R. Peng and Y. Lu, *Int. J. Hydrogen Energy*, 2013, **38**, 7430–7437.

37 Z. Salehi, S. Zinatloo-Ajabshir and M. Salavati-Niasari, *RSC Adv.*, 2016, **6**, 26895–26901.

38 S. Zinatloo-Ajabshir, Z. Salehi and M. Salavati-Niasari, *RSC Adv.*, 2016, **6**, 107785–107792.

39 C. Wang, Y. Wang, A. Zhang, Y. Cheng, F. Chi and Z. Yu, *J. Mater. Sci.*, 2013, **48**, 8133–8139.

40 F. W. Bezerra Lopes, C. P. de Souza, A. M. Vieira de Morais, J. P. Dallas and J. R. Gavarri, *Hydrometallurgy*, 2009, **97**, 167–172.

41 V. Besikiotis, C. S. Knee, I. Ahmed, R. Haugsrud and T. Norby, *Solid State Ionics*, 2012, **228**, 1–7.

42 C. Wang, W. Huang, Y. Wang, Y. Cheng, B. Zou, X. Fan, J. Yang and X. Cao, *Int. J. Refract. Met. Hard Mater.*, 2012, **31**, 242–246.

43 C. Sanchez-Bautista, A. J. Dos santos-García, J. Pena-Martínez and J. Canales-Vazquez, *Solid State Ionics*, 2010, **181**, 1665–1673.

44 S. M. Sadeghzadeh, *RSC Adv.*, 2016, **6**, 75973–75980.

45 S. M. Sadeghzadeh, R. Zhiani, M. Khoobi and S. Emrani, *Microporous Mesoporous Mater.*, 2018, **257**, 147–153.

46 S. Prabakar, K. J. Rao and C. N. R. Rao, *J. Mater. Res.*, 1991, **6**, 592.

47 S. M. Sadeghzadeh, R. Zhiani and S. Emrani, *Appl. Organomet. Chem.*, 2018, **32**, e3941.

48 S. G. Kosinski, D. M. Krol, T. M. Duncan, D. C. Douglass, J. B. Macchesney and J. R. Simpson, *J. Non-Cryst. Solids*, 1988, **105**, 45.

49 L. L. Hench, *J. Am. Ceram. Soc.*, 1991, **74**, 1487.

50 H. L. Tuller, D. P. Button and D. R. Uhlmann, *J. Non-Cryst. Solids*, 1980, **40**, 93.

51 F. Tian, L. Pan, X. Wu and F. Wu, *J. Non-Cryst. Solids*, 1988, **104**, 129.

52 M. Banach, Z. Kowalski, Z. Wzorek and K. Gorazda, *Pol. J. Chem. Technol.*, 2009, **11**, 13–20.

53 Y. Wang, H. Arandiyan, Y. Liu, Y. Liang, Y. Peng, S. Bartlett, H. Dai, S. Rostamnia and J. Li, *ChemCatChem*, 2018, **10**, 3429–3434.

54 Z. Dong, X. Le, X. Li, W. Zhang, C. Dong and J. Ma, *Appl. Catal., B*, 2014, **158–159**, 129–135.

55 N. Sahiner, H. Ozay, O. Ozay and N. Aktas, *Appl. Catal., A*, 2010, **385**, 201–207.

56 N. Sahiner, H. Ozay, O. Ozay and N. Aktas, *Appl. Catal., B*, 2010, **101**, 137–143.

57 N. Sahiner and O. Ozay, *Curr. Nanosci.*, 2012, **8**, 367–374.

58 M. H. Rashid and T. K. Mandal, *J. Phys. Chem. C*, 2007, **111**, 16750–16760.

59 Y. Chi, Q. Yuan, Y. Li, J. Tu, L. Zhao, N. Li and X. Li, *J. Colloid Interface Sci.*, 2012, **383**, 96–102.

60 S. Tang, S. Vongehr and X. Meng, *J. Phys. Chem. C*, 2009, **114**, 977–982.